

1 **Long-term Deformation Mechanism of Masjed-e-Soleyman High Rockfill Dam**

2 Morteza Salari<sup>1</sup>, Ali Akhtarpour<sup>2\*</sup>, Sajjad Khosravi<sup>3,4</sup>

3 <sup>1</sup> Department of Civil Engineering, Faculty of Engineering, Ferdowsi University of  
4 Mashhad, Iran

5 Email Address: [m.salari04@gmail.com](mailto:m.salari04@gmail.com)

6 Tel: +989156499714

7 <sup>2</sup> Department of Civil Engineering, Faculty of Engineering, Ferdowsi University of  
8 Mashhad, Iran

9 \*Corresponding author. Email address: [akhtarpour@um.ac.ir](mailto:akhtarpour@um.ac.ir)

10 [Orcid.org/0000-0003-1654-0194](https://orcid.org/0000-0003-1654-0194)

11 [Tel: +989153143978](tel:+989153143978)

12 <sup>3</sup> Department of Civil Engineering, Iran University of Science and Technology, Iran

13 <sup>4</sup> Present address : Department of Geotechnical Engineering, School of Civil  
14 Engineering, Iran University of Science and Technology, Tehran 16846-13114, Iran.

15 Email Address: [geo.sajad.406@gmail.com](mailto:geo.sajad.406@gmail.com)

16 Tel: +989398017427

17 [Orcid.org/0000-0002-4834-342X](https://orcid.org/0000-0002-4834-342X)

18 **Abstract**

19 The Masjed-e-Soleyman dam, situated in southern Iran, is a rock-fill dam with a clay  
20 core, reaching a height of 178 meters. During the construction and impounding phases,  
21 notable pore water pressure was developed within the core. The dissipation rate of this  
22 pressure is considerably slow, persisting long after impounding. Nonetheless,  
23 progressive deformations and irregularities have been observed and documented on the

24 surface of the dam's body, with no significant decrease in the rate of deformation. These  
25 deformations have raised concerns regarding the safety and stability of the  
26 superstructure. This study aims to investigate all factors influencing such deformation  
27 behavior by analyzing instrumental data and employing a mechanical-fluid three-  
28 dimensional numerical model. A modified softening-hardening constitutive model is  
29 utilized to simulate the phenomena of rock-fill particle crushing and saturated collapse  
30 within the upstream rock-fill shell materials. Additionally, a viscoelastic creep model  
31 is employed to simulate creep deformations. Subsequently, a robust hypothesis  
32 concerning the long-term mechanism of dam deformation behavior is formulated.  
33 According to this hypothesis, the main contributors to the complex behavior of this dam  
34 are the creep deformations of the rock-fill shell and the clay core's deformation under  
35 constant volume conditions.

36 **Keywords:** High rock-fill dams ‘Softening-Hardening constitutive model ‘Particle  
37 Breakage ‘Collapsed settlement ‘Creep

## 38 **1. Introduction**

39 Rock-fill materials are commonly used in the construction of dams, sourced either from  
40 river beds with rounded or sub-rounded aggregates or from rock borrow zones where  
41 sharp-edged aggregates are obtained through blasting. These materials have been  
42 extensively employed in the construction of rock-fill dams [1, 8]. Large-scale triaxial  
43 tests are commonly performed to assess the strength and deformation characteristics of  
44 rock-fill materials [9, 11]. Various constitutive models, including the non-linear elastic  
45 model [12], the elastoplastic hardening model [13], and the strain softening  
46 elastoplastic model [14], can be utilized to predict the mechanical behavior of granular  
47 materials. While linear or non-linear elastic models were previously common in  
48 simulating rock-fill behavior [15], the use of sophisticated constitutive elastoplastic

49 models based on the disturbed state idea [16] and the critical state concept [17] has  
50 become more prevalent.

51 Collapse behavior has been observed in numerous geotechnical materials based on  
52 laboratory research and field observations [18, 23]. In the case of clay-core rock-fill  
53 dams, settlement in the upstream shell can lead to increased settlement of the rock-fill  
54 shell compared to the core during the initial impounding phase. For instance, the  
55 upstream shell of the Cherry Valley dam settled four times more than the central core,  
56 resulting in longitudinal cracks on the crest and the shell-core interface [24]. Various  
57 methods have been proposed to model collapse settlement. Nobari and Duncan  
58 introduced a method that directly applies triaxial test results and is based on the  
59 hyperbolic model proposed by Duncan and Chang [12]. Another approach developed  
60 by Naylor et al. integrates the methods of Nobari and Duncan and employs a critical  
61 state elastoplastic model [25]. The Naylor technique has been applied to simulate  
62 collapse and settlement in the Beliche Dam with a rock-fill shell. Other approaches  
63 incorporate frameworks from unsaturated soil and porous medium mechanics [26]. In  
64 the context of saturated soil mechanics, Mahinroosta and Alizadeh [27] developed a  
65 method for simulating collapse settlement using a hardening/softening constitutive  
66 model. This technique was applied to model the collapse settlement of the rock-fill shell  
67 in the Gotvand Dam [28]. The effectiveness of this technique in replicating the collapse  
68 settlement of the rock-fill shell in the Masjed-e-Soleyman Dam was investigated by  
69 Akhtarpour and Salari [2].

70 Long-term deformation records of the Masjed-e-Soleyman Dam in southwest Iran  
71 reveal significant creep behavior in its rock-fill structure. Despite the stress state  
72 remaining unchanged, the dam continues to deform long after its completion [29]. This  
73 macroscopic creep behavior can be attributed to the subcritical propagation of cracks

74 within stressed particles [30]. Extensive laboratory and in-situ experiments have been  
75 conducted to study the creep behavior of rock-fill materials [31, 32] and rocks [33, 34].  
76 The findings suggest that rock-fill creep, characterized by continuous crushing, is  
77 influenced by various factors such as rock type, mineralogical composition, grain size  
78 distribution, stress state at grain contacts, initial density, particle characteristics,  
79 moisture content, time-dependent degradation of solid hardness due to chemical  
80 reactions, and environmental factors like temperature and freeze-thaw actions. Based  
81 on these experimental findings, several constitutive models have been proposed,  
82 employing a continuum approach that relates time to long-term strain through a  
83 logarithmic relationship [35].

84 The Masjed-e-Soleyman Dam is a 178-meter high rock-fill dam with a central core.  
85 Despite extensive research [2], the long-term deformation behavior of this dam remains  
86 complex and challenging to fully understand. Instrumentation records show significant  
87 pore water pressure during construction and initial impounding, which dissipates very  
88 slowly, taking about 14 years. Although minimal consolidation-induced deformation in  
89 the core was expected, the dam body has exhibited substantial and continuous  
90 deformations, including significant subsidence of the crest, longitudinal berm-like  
91 subsidence on the upstream surface, and extensive tensile cracks near the crest and  
92 abutments. These ongoing deformations pose concerns about the long-term safety and  
93 stability of the structure.

94 The rock-fill shells of the dam consist of conglomerate with calcareous cement  
95 components. Previous studies have demonstrated that the strength and deformation  
96 behavior of rock-fill materials are influenced by particle size distribution, rotation,  
97 particle breakage, and re-arrangement. These factors have contributed to notable  
98 subsidence in the upstream shell of the dam caused by saturation during the initial

99 impounding, as well as long-term creep deformations in the rock-fill shell [2]. In this  
100 study, by analyzing data obtained from the dam instrumentation system and employing  
101 three-dimensional numerical simulations, the primary causes underlying its complex  
102 deformation behavior are identified, and the most plausible hypothesis is presented.

## 103 **2. Masjed-e-Soleyman dam (MES Dam)**

104 The Masjed-e-Soleyman Dam, previously known as "Godar-e-Landar," is a rock-fill  
105 dam located on the Karun River in southwest Iran. It has a reservoir capacity of 261  
106 million cubic meters and generates 2000 MW of electricity. The primary cross-section  
107 of the dam, has a crest length of 500 meters and a width of 15 meters. The surrounding  
108 rock mass consists of alternating layers of siltstone and conglomerate from the Aghajari  
109 and Bakhtyari formations. The dam was constructed in a narrow valley with wall slopes  
110 averaging 36 degrees.

111 Site evaluations identified the Simband borrow area as the ideal source of materials for  
112 the dam's core. The borrow area contains layers of clay (CL) and clayey gravel (GC)  
113 distributed irregularly. The upper one-third of the core was compacted with a water  
114 content below the optimum level, while the lower two-thirds were compacted with a  
115 water content exceeding the optimum level. The dam's shells are made of compressed  
116 conglomerate rock fill obtained through blasting, with insufficient moisture content.  
117 Regions 3A and 3C have coarser aggregates compared to area 3B. Properly graded  
118 conglomerate aggregates are present in the filter zones (2A, 2B, and 2C).

119 To monitor stress, pore pressure, and settlement within the dam, various instruments  
120 were strategically positioned at chainages (CH.) 160, 260, 360, and 420 meters from  
121 the left side of the crest's end. However, significant deformations during the final 50  
122 meters of embankment construction damaged many of these instruments, including  
123 Electrical Piezometers (EP), Total Pressure Cells (TPC), and magnetic plates (MP). At

124 CH. 260 in the primary cross-section (Fig. 1-Supplementary), the instruments remained  
125 intact. Each cluster (C) in this cross-section includes three horizontally installed TPCs  
126 tilted at 45 degrees upward and 45 degrees downward, along with a single EP.  
127 Additionally, a system of survey measurement points (SMP) was established on the  
128 dam to monitor surface displacements approximately one month after the first  
129 impounding began, when the water reservoir level had risen by around 57 meters (refer  
130 to Fig. 2- Supplementary).

### 131 **3. Dam Monitoring during a long-term period**

132 During the construction of the Masjed-e-Soleyman Dam, the generated fill load  
133 increased vertical stress, causing elevated excess pore water pressure and deformation.  
134 The first impounding introduced water pressure on the core and foundation, with  
135 buoyancy forces and saturation collapse occurring in the upstream shell due to water  
136 ingress [36]. Significant excess pore water pressure was observed during construction,  
137 mainly due to the rapid construction rate and low permeability of the core. Minor  
138 changes in the pore water pressure ratio (PWP) over time suggest minimal dissipation  
139 of excess pressure even 14 years after impounding.

140 The core's permeability decreases exponentially with increased effective vertical stress,  
141 leading to long-term dissipation of excess pore pressure, especially near the filters [2].

142 In the lower parts of the core, the PWP and stress ratios ( $r_u$  and  $r_k$ ) approach unity,  
143 indicating a quasi-fluid behavior due to high excess pore water pressure and almost  
144 incompressible conditions.

145 After the completion of the initial impounding of the Masjed-e-Soleyman Dam,  
146 significant rotations in the direction of the principal stresses were observed in the main  
147 cross-section. Above level 270, the stresses rotated anti-clockwise, while below level  
148 230, a clockwise rotation was noted, reflecting complex stress behaviors. Shear

149 movements in the dam were associated with contractive behavior, influencing the  
150 overall stability of the structure.

151 Measurements from magnetic plates (MPs) and survey points indicated notable  
152 deformations. For instance, during construction, the core experienced a maximum  
153 settlement of 3.7 meters, a behavior that contrasts with the expected slow consolidation  
154 characteristic of the core. Additional settlements of up to 2.2 meters were observed at  
155 the crest during the initial impounding, primarily driven by high excess pore water  
156 pressure rather than consolidation.

157 The SMP was installed one month after the first impounding to assess surface  
158 displacements. Half of the total settlement occurred during the initiation of the first  
159 impounding, with settlements in the upstream shell being a significant factor  
160 influencing the deformation behavior during the first impounding. The temporal  
161 variation in settlement and horizontal displacement (perpendicular to the dam axis) of  
162 surface measurement points, situated in the maximum cross-section of the dam, are  
163 illustrated in Fig. 1 and 2 (Fig. 1- Supplementary and 2- Supplementary show the  
164 corresponding locations). As reported by Hunter (2003) [24] in regards to surface  
165 deformations observed in rock-fill dams during the post-construction phase (Fig. 3), the  
166 SMP21 benchmark is situated in zone three, which experiences the most significant  
167 impact from deformations in the upstream shell. Similarly, SMP22, located in region  
168 two, is primarily influenced by deformations in the core. Fig. 1 and 2 demonstrate a  
169 nearly identical magnitude and rate of deformations at these two points, signifying a  
170 similar deformation behavior for the dam core and the upstream shell at upper  
171 elevations. Over a period of 14 years since the commencement of impoundment, the  
172 deformations within these regions exhibit an increasing trend. Remarkably, the  
173 maximum settlement recorded on the dam surface, since the conclusion of

174 impoundment, amounts to 3.01 meters in these areas. It is important to note that these  
175 deformations are unrelated to the consolidation mechanism due to the negligible  
176 dissipation of excess pore pressure within the core.

177

178 On the downstream surface, the deformations at SMP23 and SMP24, located  
179 respectively at heights of 0.8 and 0.6 within the primary section of the dam, are more  
180 influenced by deformations in the downstream rock-fill shell. While these points  
181 demonstrate the highest horizontal displacements (1.3 m) since the end of impounding,  
182 their settlements are one-third of those observed at crest points. Given that the dam shell  
183 consists of rock-fill materials, it is the phenomenon of creep that governs their long-  
184 term deformation behavior. Consequently, creep deformations in the shell materials  
185 play a crucial role in the long-term deformation mechanism of the dam.

186 SMP25, located in the lower portion of the dam shell, is most susceptible to  
187 deformations originating from the dam foundation. However, the deformation at this  
188 point is minimal, as depicted in Fig. 2. In order to assess the deformation characteristics  
189 of the underlying rock foundation, a series of measurement points were installed inside  
190 the dam inspection gallery, situated on the rock foundation below the core and dam  
191 axis, in 2010, eight years after the initial impoundment. The variation of surface  
192 settlement from early 2010 to 2015 is presented in Fig. 4. The maximum settlement  
193 recorded within the inspection gallery (on the rock) over a period of approximately five  
194 years amounted to 7 mm, while during the same timeframe, the settlement at the crest  
195 point (SMP21) reached approximately 1.5 meters (see Fig. 1). Additionally, in January  
196 2006, a set of in-place electrical inclinometers (INC) was installed at the main section  
197 of the dam downstream of the core through drilling operations to evaluate the  
198 deformation interaction between the shell, core, and foundation. The location of this



199 inclinometer and the profiles of horizontal displacement recorded since installation are  
200 shown in Fig. 5. It is evident that the magnitude of lateral deformations at levels  
201 adjacent to the foundation is negligible and increases with height. Based on these  
202 observations, it can be concluded that the deformations in the foundation of the MES  
203 dam are minimal compared to those exhibited by the dam body, indicating that the  
204 foundation does not exert a decisive influence on the long-term deformation mechanism  
205 of the dam. On the contrary, the increase in lateral deformations with increased height  
206 confirms that creep phenomenon in rock-fill shells can significantly impact the dam's  
207 long-term deformation behavior.

#### 208 **4. Numerical modeling**

209 The investigation of dam behavior was conducted through three-dimensional modeling  
210 using the FLAC 3D program, as illustrated in Fig. 6. The modeling employed the finite  
211 difference method, utilizing 75,600 hexahedral tetrahedral elements. In order to ensure  
212 modeling accuracy, the dimensions of element edges, model dimensions, and geometric  
213 boundaries of the lateral and bottom aspects of the numerical model were selectively  
214 chosen to avoid impacting the modeling results. The analysis encompassed the  
215 simultaneous consideration of flow-mechanical formulation. Specifically,  
216 consolidation in the core, collapse in the upstream rock-fill material, and creep in the  
217 upstream and downstream rock-fill material were taken into account during the  
218 construction period, first impoundment, and long-term period, respectively.

219 During the initial impounding and construction phases, the mechanical behavior of  
220 materials was simulated using the elastoplastic hardening/softening constitutive model  
221 (See Appendix). This constitutive model implements the elastic modulus based on the  
222 Duncan and Chang equation [12], which has been validated by numerous researchers  
223 (2020). Frictional hardening and dilatancy behavior were simulated using the modified

224 equation proposed by Vermeer and de Borst [37], as well as the modified equation  
225 proposed by Rowe [38] and further modified by Akhtarpour and Salari [2].

226 In order to obtain parameters for the modified constitutive model used in the dam  
227 materials, conventional triaxial tests were conducted on core samples. Additionally,  
228 large-scale triaxial tests were performed at Karlsruhe University on the coarse-grained  
229 materials found in the shell, filter, and drainage regions of the dam [2].

230 To determine the parameters of the materials used in the dam body, conventional and  
231 large-scale triaxial tests were simulated using the FLAC software platform. The  
232 constitutive model was implemented with all relevant functions and equations using the  
233 FISH programming language within the software. The simulations utilized a single  
234 element with axial symmetry and appropriate boundary conditions. During each stage  
235 of analysis, the program calculated the plastic shear strain and updated the model  
236 parameters based on the defined functions and equations. (For calibration details under  
237 diverse conditions see Fig. 3- Supplementary)

238 The final parameters are presented in Table 2. In this analysis, the cohesion value is  
239 determined based on the distance between the origin of the tangent line and Mohr's  
240 circles. As presented in Table 2, the exponent ( $n$ ) for regions 3A and 3C under initial  
241 dry conditions exhibits a negative value, indicating that an increase in confining stress  
242 causes a decrease in Young's modulus. These regions, characterized by more extensive  
243 breakage compared to others, display the highest values of  $I_d$ . The fine-grained nature  
244 of the core materials poses challenges for breakage, resulting in an  $I_d$  value of 1 for  
245 these materials.

246 The surrounding rock mass was modeled using a linear elastic constitutive model, and  
247 the corresponding parameters can be found in Table 3. The FLAC3D software [39]

248 employed a flow-mechanical formulation that incorporates a permeability function  
 249 dependent on the effective vertical stress, as proposed in Eq. 1.

$$K_{int(y)} = \begin{cases} 2 \times 10^{-8} \\ 1.82 \times 10^{-6} \left( \frac{\sigma'_y}{P_a} \right)^{-0.48} \end{cases} \quad \frac{K_{int(x)}}{K_{int(y)}} = 2.5 \quad \text{Eq.1}$$

250 Where  $K_{int(x)}$  and  $K_{int(y)}$  are the horizontal and vertical saturated permeability  
 251 coefficients (cm/s), and  $\sigma'_y$  is the effective vertical stress (kPa).

252 After the initial impounding, the mechanical response of the rock-fill materials was  
 253 analyzed employing a visco-plastic constitutive model known as Cvisc within the  
 254 FLAC3D software. The Cvisc model in FLAC3D exhibits a visco-elastoplastic  
 255 behavior in terms of both deviatoric and volumetric response. It is assumed that the  
 256 visco-elastic and plastic strain-rate components act sequentially. Specifically, the visco-  
 257 elastic constitutive law follows the Burgers model, consisting of a Kelvin unit  
 258 connected in series with a Maxwell component, while the plastic constitutive law  
 259 incorporates the Mohr-Coulomb model. For the sake of consistency within this section,  
 260 the symbols  $s_{ij}$  and  $e_{ij}$  are employed to represent the deviatoric stress and strain  
 261 components, respectively.

$$s_{ij} = \sigma_{ij} - \sigma_0 \delta_{ij} \quad \text{Eq.2}$$

$$e_{ij} = \varepsilon_{ij} - \frac{e_{vol}}{3} \delta_{ij} \quad \text{Eq.3}$$

262 Where:

$$\sigma_0 = \frac{\sigma_{kk}}{3} \quad \text{Eq.4}$$

263 And

$$e_{vol} = \varepsilon_{kk} \quad \text{Eq.4}$$

264 Also, Kelvin, Maxwell, and plastic contributions to stresses and strains are labeled  
 265 using  $K$ ,  $M$ , and  $P$ , respectively. Strain rate partitioning:

$$\dot{e}_{ij} = \dot{e}_{ij}^K + \dot{e}_{ij}^M + \dot{e}_{ij}^P \quad \text{Eq.5}$$

266 Kelvin:

$$S_{ij} = 2\eta^K \dot{e}_{ij}^K + 2G^K \dot{e}_{ij}^K \quad \text{Eq.6}$$

267 Maxwell:

$$\dot{e}_{ij}^M = \frac{\dot{S}_{ij}}{2G^M} + \frac{S_{ij}}{2\eta^M} \quad \text{Eq.7}$$

268 Mohr-Coulomb:

$$\dot{e}_{ij}^P = \lambda^* \frac{\partial g}{\partial \sigma_{ij}} - \frac{1}{3} \dot{e}_{vol}^P \delta_{ij} \quad \text{Eq.8}$$

$$\dot{e}_{vol}^P = \lambda^* \left[ \frac{\partial g}{\partial \sigma_{11}} + \frac{\partial g}{\partial \sigma_{22}} + \frac{\partial g}{\partial \sigma_{33}} \right] \quad \text{Eq.9}$$

269 In turn, the volumetric behavior is given by

$$\dot{\sigma}_0 = K \left( \dot{e}_{vol} - \dot{e}_{vol}^P \right) \quad \text{Eq.10}$$

270 Within these equations, the parameters  $K$  and  $G$  represent the bulk modulus and shear  
 271 modulus, respectively, while  $\eta$  denotes the dynamic viscosity (obtained by multiplying  
 272 the kinematic viscosity with mass density). The Mohr-Coulomb yield envelope  
 273 incorporates both shear and tensile conditions. The yield criterion is defined as  $f = 0$ ,  
 274 wherein the principal axes formulation yields the following: Shear yielding:

$$f = \sigma_1 - \sigma_3 N_\varphi + 2C \quad \text{Eq.11}$$

275 Tension yielding:

$$f = \sigma^t - \sigma_3 \quad \text{Eq.12}$$

276 Where  $C$  is the material cohesion,  $\varphi$  is the friction,  $N_\varphi = \frac{1 + \sin \varphi}{(1 - \sin \varphi)}$ ,  $\sigma^t$  is the tensile  
 277 strength, and  $\sigma_1$  and  $\sigma_3$  are the minimum and maximum principal stresses (compression  
 278 negative).

279 Shear failure:

$$g = \sigma_1 - \sigma_3 N_\psi \quad \text{Eq.13}$$

280 Tension failure:

$$g = -\sigma_3 \quad \text{Eq.14}$$

281 Where  $\psi$  is the material dilation and  $N_\psi = \frac{1 + \sin \psi}{(1 - \sin \psi)}$ . Finally,  $\lambda^*$  is a nonzero parameter

282 during plastic flow only, which is determined by applying the plastic yield condition  $f$   
 283  $= 0$ .

284 The main parameters of described creep model are Bulk modulus (K) (Elastic  
 285 volumetric response – no creep), Kelvin viscosity ( $\eta^K$ ), Kelvin shear modulus ( $G^K$ ),  
 286 Maxwell viscosity ( $\eta^M$ ), Maxwell shear modulus ( $G^K$ ), Cohesion ( $C$ ), Angle of  
 287 friction ( $\varphi$ ), Angle of dilation ( $\psi$ ).

288 Particle breakage (PSD, particle breakage, rotation, and re-arrangement) of rock-fill  
 289 particles over time, due to forming micro-cracks and changes in moisture content, are  
 290 the main cause of creep deformation in these materials. These phenomena cause  
 291 changes in the strength properties and deformability of these materials. Due to the  
 292 anisotropic creep properties of rock-fill materials, large-scale accurate testing that can  
 293 determine the main creep properties of rock-fill materials is so complex and expensive.

294 This creep test has not been performed on the rock-fill materials of Masjed-e-Soleyman  
295 Dam. Therefore, in this study, the creep model parameters are determined based on the  
296 results of triaxial tests and analysis trials. Table 4 shows the determined parameters.

297 The parameters of cohesion ( $C$ ), friction angle ( $\phi$ ), and dilation angle ( $\Psi$ ) are  
298 determined directly based on the results of triaxial tests (Table 2). With the help of  
299 parameters ( $K, n, \nu$ ) in Table 2, the bulk modulus ( $K$ ) and Maxwell shear modulus ( $G^M$   
300 ), were determined (Using Eq. 5 in appendix,  $G^M = E/2(1+\nu)$ ,  $K = E/3(1-2\nu)$ ). The other  
301 values of creep parameters are determined based on analysis trials. Surface  
302 displacements and long-term settlement of survey measurement points (SMP) located  
303 between 0.8 and 0.6 of the dam heights from the crest axis (SMP23 in Fig. 2-  
304 Supplementary) have been selected for determining these creep parameters.

## 305 **5. Sequence and calibration of modeling**

306 The construction of the dam was completed in November 2000, following a period of  
307 approximately five years. Forty-two layers were employed in the simulation to replicate  
308 the placement process. The initial filling of the reservoir commenced one month after  
309 the completion of construction. During the initial filling, the water level in the reservoir  
310 was set at +255. The simulation accounts for impounding effects and collapse  
311 settlement, as discussed by Akhtarpour and Salari (2020) [2] and Mahin Roosta et al.  
312 (2012) [27]. Mahin Roosta and Alizadeh (2012) [27] proposed a stress reduction  
313 coefficient to mitigate the effective compressive stress components in the recently  
314 saturated layer. The influence of confining pressure on the collapse phenomenon [40],  
315 as well as the stress reduction coefficient ( $C_c$ ) derived from trial analyses for each  
316 impounding stage, has been observed by several researchers (refer to Table 5).

317 After modeling the initial impounding, the constitutive model for the dam shell material  
318 was updated to include the Cvisc creep model, allowing the simulation of long-term

319 deformation by accounting for creep phenomena in the rock-fill shell materials and  
320 consolidation in the core. The simulation results showed a strong correlation between  
321 calculated pore pressure values and deformation patterns in the dam and the actual  
322 measured data from the central cross-section. This alignment between the simulated  
323 and observed values demonstrates the model's effectiveness in accurately replicating  
324 the dam's long-term behavior under creep and consolidation conditions. (See Fig. 4–  
325 Supplementary to 8–Supplementary)

## 326 **6. Numerical Results and discussion**

327 The pore pressure contours in CH.260 reveal that excess pore pressure did not develop  
328 in the upper portions of the core, while high excess pore pressure was observed in the  
329 lower sections due to the core's low permeability and high construction rate. At the  
330 lower levels, a nearly constant excess pore pressure was maintained between the core's  
331 center and upstream or downstream locations. Fig. 7, showing pore water pressure at  
332 September 2016, highlights the persistent high excess pore pressure in these lower  
333 areas, indicating the slow dissipation of pressure over time. (For details on pore pressure  
334 at the end of construction and the end of the first impounding, please refer to Fig. 9-  
335 Supplementary and 10-Supplementary.)

336 During the initial impounding, the core experienced nearly undrained conditions,  
337 leading to negligible dissipation of pore pressure from the end of the first impounding  
338 until the end of the analysis. The slow dissipation of excess pore pressure and high  
339 generation of pore water pressure in the lower part of the core created a quasi-fluid zone  
340 with zero effective stress. Effective vertical stresses decreased during impounding due  
341 to buoyancy forces in the upstream shell. The undrained nature of the core caused an  
342 increase in total stress due to water pressure on the upstream side, reducing the size of  
343 regions with zero effective stress near the upstream. Fourteen years after the first

344 impounding, a slight decrease in excess pore pressure led to an increase in effective  
345 stress, reducing the extent of the zero effective stress zone compared to earlier phases.  
346 Fig. 8, which shows pore water pressure at September 2016, illustrates this behavior  
347 clearly. (Refer to Fig. 11-Supplementary and 12- Supplementary for stress data at  
348 earlier stages.)

349 At the end of the first impounding, shear strain contours in the central cross-section  
350 indicated the generation of shear zones due to the placement of the embankment's upper  
351 parts. These zones further developed as a result of differential deformations between  
352 the upstream shell and core, along with water pressure effects on the core. Increased  
353 shear strain in the upstream core led to the formation of hydraulic cracks and contractive  
354 behavior, causing a rise in pore water pressure. During long-term creep deformation,  
355 particularly lateral creep towards the outer body, additional space was created for the  
356 core to deform in both directions, resulting in pronounced plastic shear deformations.  
357 Additionally, principal stresses in the central cross-section at the end of the first  
358 impounding showed significant rotation due to oblique shear zones, with similar stress  
359 magnitudes observed near the filter regions and central core. This stress behavior  
360 underscores the complex interactions within the dam structure during and after  
361 impounding.

362 The upper sections of the dam adjacent to the abutments experience tensile stress,  
363 resulting in the development of transverse tensile cracks (Fig. 9). The extent of these  
364 tensile areas corresponds to the observed cracks on the crest. Based on the modeling  
365 results in September 2016, the maximum depth of the area with tensile stress in the core  
366 next to the right and left supports is 4.5 and 6 meters, respectively, relative to the crest  
367 level. Therefore, an important long-term issue that may affect the dam's safety is the



368 increasing depth of tension cracks in the core near the valley walls. This could  
369 potentially lead to internal erosion due to reservoir water leakage into these areas.

370 Vertical and horizontal displacements, along with the deformed mesh in the central  
371 cross-section at the completion of construction, show that settlement from  
372 consolidation was negligible due to the slow accumulation of excess pore pressure and  
373 the high excess pore pressure in the dam's lower regions during construction.

374 Settlements in the shell were primarily influenced by variations in particle size  
375 distribution, breakage, rotation, and re-arrangement. Lateral deformations were also  
376 noted in the lower sections of the dam body, driven by oblique shear zones. (Refer to  
377 Fig. 13-Supplementary to 15-Supplementary)

378 Figs. 10-11 depict the outcomes of the end of the first impounding, showcasing the  
379 vertical and horizontal displacements. The maximum vertical displacement within the  
380 dam reaches 5.93 meters, while displacement at the crest is measured at 2.2 meters.

381 Differential settlements are particularly noticeable at the upper regions of the interface  
382 between the shell and core on the upstream side. Water pressure on the upstream face  
383 contributes to smaller lateral deformations in the lower sections of the core compared  
384 to those observed during construction. A berm-like subsidence is evident in the upper  
385 portions of the upstream side of the dam, consistent with on-site observations. These  
386 collapse settlements in the upstream rock-fill shell are identified as the primary cause  
387 of the observed deformation behavior during the first impounding phase. The contour  
388 distribution of settlement and horizontal deformation within the central cross-section at  
389 the end of the first impounding in September 2016 is depicted in Figs. 12 and 13.

390 Furthermore, Figs. 14 to 16 exhibit the contour distribution of settlement, horizontal  
391 deformation perpendicular to the dam axis, and horizontal deformation parallel to the  
392 dam axis on the three-dimensional model surface after the first impounding phase.

393 During the period from the end of impounding to September 2016, the maximum  
394 settlement of the dam crest is 3.1 meters, primarily occurring in the middle sections of  
395 the crest. The maximum horizontal deformation perpendicular to the dam axis is 1.9  
396 meters, which is supported by field data and evidence. Throughout this period, the  
397 overall deformation behavior of the dam shells is directed towards the outer areas.  
398 However, the upper levels of the upper shell exhibit downward deformation, contrary  
399 to the lower levels. This deformation pattern results in a berm-like deformation  
400 complication in the upper sections upstream of the dam, aligning with field  
401 observations. The lower parts of the core experience lateral deformation towards the  
402 shells (bulging) due to the horizontal movements of the shell, while the upper parts of  
403 the core and shell subside. Furthermore, the geometric shape of the valley influences  
404 horizontal deformation towards the middle sections of the valley.

405 Fig. 17 depicts the deformed mesh of the main section of the dam, while Fig. 18  
406 provides a three-dimensional view of the deformed mesh in September 2016 relative to  
407 the end of the first impounding. These figures reveal complications such as berm-like  
408 deformation on the upstream surface of the dam, core bulging at lower levels, and  
409 significant settlement in the middle parts of the dam crest.

410 Based on the aforementioned explanations, it can be concluded that the general  
411 mechanism behind the long-term deformation behavior of the MES dam is as follows:

412 "The significant pore pressure generated in the core, coupled with the low permeability  
413 of the materials, results in almost undrained conditions in the lower levels of the dam  
414 core. The rock-fill materials in the dam shells possess a high potential for particle  
415 crushing, leading to substantial creep deformations over time. The creep deformations  
416 of the shell material towards the outer areas of the dam cause lateral deformation of the  
417 lower parts of the core towards the shells. The deformation behavior of the core at the

418 lower levels, under constant volume conditions and the formation of shear zones, causes  
419 simultaneous settlement in the upper sections of both the body and the core."

420 Fig. 19 illustrates the complex deformation mechanisms in the dam, highlighting  
421 settlement, creep, shear, and bulging effects. Settlement in the upper regions results  
422 from material compaction and consolidation under sustained loads. Creep deformation,  
423 shown by yellow arrows, represents the time-dependent lateral and vertical movements  
424 in the rock-fill shell, driven by stress conditions and environmental factors. A zero  
425 effective stress region within the core, marked by an outlined oval, exhibits quasi-fluid  
426 behavior due to high pore water pressure, contributing to ongoing deformation. Shear  
427 zones indicated by red lines show differential movements between the core and shell,  
428 leading to potential cracking and hydraulic fracturing. Bulging directions in the core,  
429 depicted by blue arrows, indicate outward deformation under lateral stresses.

## 430 **7. Conclusions**

431 This research aims to explain the long-term deformation behavior of the MES dam from  
432 the end of impounding to September 2016. Data from instruments and a mechanical-  
433 fluid three-dimensional numerical model were used to analyze the factors influencing  
434 deformation behavior. The key findings are as follows:

435 1) Excess pore pressure dissipates slowly during this period, resulting in minimal  
436 settlement from consolidation. The lower parts of the core exhibit nearly  
437 incompressible behavior.

438 2) Deformations in the rockfill dam, as observed through surface mapping points,  
439 micro-geodetic points in the underground gallery, and deviation meter  
440 measurements inside the downstream shell, have a negligible impact on long-  
441 term deformation behavior.

442 3) The creep behavior of rock-fill shell materials significantly contributes to the

443 deformation behavior of the dam during this period. Creep deformations in the  
444 shell material perpendicular to the dam's axis cause lateral deformation  
445 (bulging) in the lower regions of the core. The almost incompressible and  
446 undrained behavior of the lower parts of the core leads to settlement in the upper  
447 parts of the core and shells. This hypothesis provides a strong explanation for  
448 the mechanism of dam deformation behavior in the long term (see Fig. 19). The  
449 majority of settlement occurs on the dam crest, while surface deformation  
450 perpendicular to the dam's axis is most pronounced on the downstream shell.

451 4) The deformation mechanism results in upward movement of the upper parts of  
452 the upstream shell and downward movement of the lower parts, leading to a  
453 berm-like complication in the upper levels of the upstream shell.

454 5) The dam body experiences horizontal deformation towards the middle sections  
455 due to significant settlement in the central cross-section. This results in areas  
456 with tensile stresses adjacent to the valley walls. Based on modeling results in  
457 September 2016, the maximum depth of the area with tensile stress in the core  
458 adjacent to the right and left abutments is 4.5 and 6 meters relative to the crest  
459 level, respectively.

460 6) This study confirms that the phenomenon of creep deformation in the used  
461 materials of rockfill, such as those used in tall structures like rockfill dams, can  
462 play a determining role in the long-term deformation behavior of these  
463 structures. Additionally, the creation and development of significant excess  
464 pore pressure in the clay core of tall rockfill dams can be another major  
465 influential factor in these particular megastructures.

466 Currently, there is no evidence of a significant reduction in the deformation rate of the  
467 Masjed-e-Soleyman dam, and these deformations due to the creep phenomenon in the

468 rock-fill shell material may continue with the proposed mechanism for several decades  
469 after dewatering. In these conditions, one of the issues that may affect the long-term  
470 safety of the dam is the increase in the depth of tension cracks in the core of the dam in  
471 areas adjacent to the valley walls. With the penetration of reservoir water into these  
472 areas, the occurrence of internal erosion is likely. Another risk that can affect the dam's  
473 safety is the reduction in height due to significant settlement on the dam crest.  
474 However, predicting the deformation behavior of the dam in the future, with the  
475 proposed deformation mechanism in this article, can become the subject of future  
476 studies and research by identifying hazards and destabilizing factors of the dam, as well  
477 as providing remedial solutions.

478

479 **Appendix : Mechanical Constitutive model**

480 A numerical simulation was conducted using FLAC3D software to analyze the mechanical  
481 behavior of the dam's materials. The simulation utilized an elasto-plastic hardening/softening  
482 constitutive model based on the Mohr-Coulomb model. This model accurately captures the initial  
483 elastic response of the materials by incorporating Young's modulus (E) and Poisson's ratio ( $\nu$ ).  
484 Subsequently, the model accounts for the hardening/softening and dilative behavior of the  
485 materials by considering parameters such as friction angle, cohesion, dilation angle, and tensile  
486 strength as functions of plastic shear strain and tensile strain, until they reach their maximum  
487 values.

488 **Yield envelopes and potential functions**

489 The yield surface functions of this constitutive model were mathematically defined by Eqs. (1) and  
490 (2).

$$f^s = \sigma_1 - \sigma_3 \frac{1 - \sin \phi_m}{1 + \sin \phi_m} + 2c_m \sqrt{\frac{1 - \sin \phi_m}{1 + \sin \phi_m}} \quad \text{Eq. 1}$$

$$f^t = \sigma_m^t - \sigma_3 \quad \text{Eq. 2}$$

491 In the following set of equations, the variables  $f^s$  and  $f^t$  denote the shear and tensile yield  
492 functions, respectively. The variables  $\sigma_1$  and  $\sigma_3$  represent the maximum and minimum principal  
493 stresses. Additionally,  $\phi_m$ ,  $c_m$  and  $\sigma_m^t$  signify the mobilized friction angle, mobilized cohesion,  
494 and mobilized tensile strength of the model, respectively.

495 The non-associated flow rule was adopted for shearing, while the associated flow rule was  
496 employed for tension. The plastic potential functions were defined as follows:

$$Q^s = \sigma_1 - \sigma_3 \frac{1 - \sin \psi_m}{1 + \sin \psi_m} \quad \text{Eq. 3}$$

$$Q^t = -\sigma_3 \quad \text{Eq. 4}$$

497 In the presented set of equations, we introduce the variables  $Q^S$  and  $Q^t$ , which represent the shear  
 498 and tensile plastic potential functions, respectively. Furthermore,  $\psi_m$  denotes the mobilized  
 499 dilation angle.

### 500 **Stress-dependent elastic modulus**

501 In the majority of geotechnical materials, it is observed that the elastic modulus is influenced by  
 502 the confining stress. Consequently, to account for this dependency, Equation (5) proposed by  
 503 Duncan and Chang (1970) in their hyperbolic (nonlinear elastic) model is incorporated into the  
 504 constitutive model. This equation serves to define and represent the relationship between the  
 505 elastic modulus and the confining stress.

$$E = KP_a \left( \frac{\sigma_3}{P_a} \right)^n \quad \text{Eq. 5}$$

506 The equation presented herein introduces various parameters related to the elastic behavior of  
 507 materials in civil engineering. In this context, E represents Young's modulus, K denotes the elastic  
 508 modulus,  $P_a$  signifies the atmospheric pressure, and n represents the exponent governing the  
 509 dependence of the elastic modulus on the confining stress. Furthermore, the Poisson's ratio ( $\nu$ ) is  
 510 considered as a constant value in this study. The combination of these elasticity parameters ensures  
 511 an appropriate response within the elastic domain of the constitutive model.

### 512 **Frictional hardening**

513 Vermeer and de Borst (1984) [37] put forward a formulation describing the frictional hardening  
 514 behavior of geotechnical materials. This formulation accounts for the variation of the mobilized  
 515 friction angle, denoted as  $\phi_m$ , with respect to the plastic shear strain, exhibiting a gradual increase  
 516 towards its peak value  $\phi_p$ . Building upon this work, Mahinroosta et al. (2015) [28] introduced a

517 modification to the aforementioned relation by considering an initial mobilized friction angle,  $\phi_0$ .

518 The resulting modified equation is presented below:

$$\sin \phi_m = \begin{cases} \sin \phi_0 + 2 \frac{\sqrt{\varepsilon_s^p \times \varepsilon_s^f}}{\varepsilon_s^p + \varepsilon_s^f} (\sin \phi_p - \sin \phi_0) & \text{for } \varepsilon_s^p \leq \varepsilon_s^f \\ \sin \phi_p & \text{for } \varepsilon_s^p > \varepsilon_s^f \end{cases} \quad \text{Eq. 6}$$

519 Within the given equation, the plastic shear strain is represented by  $\varepsilon_s^p$ , while  $\varepsilon_s^f$  denotes the  
 520 plastic shear strain at the peak friction angle. An important parameter, denoted as  $\phi_0$ , plays a  
 521 significant role in determining the range of elastic behavior that materials exhibit. This parameter  
 522 is known to be influenced by the confining stress and can be defined as a function thereof.

### 523 Dilatancy behavior

524 In the field of geotechnical engineering, Rowe (1963) [38] put forward Eq. 7 to explain the  
 525 phenomenon of dilatancy hardening exhibited by geotechnical materials.

$$\sin \psi_m = \frac{\sin \phi_m - \sin \phi_{cv}}{1 - \sin \phi_m \sin \phi_{cv}} \quad \text{Eq.7}$$

526 In the context of civil engineering, the parameter  $\psi_m$  represents the mobilized dilation angle, while  
 527  $\phi_{cv}$  corresponds to the critical state friction angle or the friction angle of constant volume. This  
 528 critical state friction angle value can be determined by utilizing Eq. 8.

$$\sin \phi_{cv} = \frac{\sin \phi_p - \sin \psi_p}{1 - \sin \phi_p \sin \psi_p} \quad \text{Eq. 8}$$

529 In the realm of civil engineering, the peak dilation angle denoted as  $\psi_p$  assumes significance. To  
 530 refine Rowe's stress-dilatancy equation for rockfill material, formulation is simplified and revised  
 531 as presented below:

$$\sin \psi_m = R_d \frac{\sin \phi_m - \sin \phi_{cv}}{1 - \sin \phi_m \sin \phi_{cv}} \quad \text{Eq. 9}$$

532 In the aforementioned equation,  $R_d$  is incorporated as a reduction factor with a value less than one,



533 representing the influence of particle size distribution (PSD), particle breakage, rotation, and  
 534 rearrangement on the deformation behavior of rockfill material. In their recent study, Akhtapour  
 535 and Salari (2020) [2] introduced Eq. 10 as a more comprehensive alternative to Eqs. 7 and 9.

$$\sin \psi_m = \begin{cases} \sin(I_c \cdot \psi_{mR}) & -90 \leq I_c \cdot \psi_{mR} \leq 0 \\ \sin(R_d \cdot \psi_{mR}) & 0 < R_d \cdot \psi_{mR} \leq 90 \end{cases} \quad \text{Eq. 10}$$

536 In the aforementioned equation,  $\psi_{mR}$  represents the mobilized dilation angle acquired through the  
 537 utilization of Rowe's equation, expressed in degrees.  $I_c$  denotes the contraction factor, a value  
 538 exceeding zero and potentially surpassing unity. This factor serves as an appropriate metric for  
 539 quantitatively evaluating the magnitude of the influences exerted by PSD, particle breakage,  
 540 rotation, and rearrangement on the deformation of rockfill materials throughout the contraction  
 541 phase.

#### 542 **Stress dependent peak friction and dilation angle**

543 The experimental analysis conducted in the laboratory has revealed that the ultimate friction angles  
 544 are influenced by the applied confining pressure. Consequently, this interrelation is taken into  
 545 consideration in the constitutive model through the implementation of Eq. 11. The stress-  
 546 responsive friction angle, as determined, is utilized as the upper limit for friction in Eq. 8.

$$\phi_p = \phi_s - \Delta\phi \log\left(\frac{\sigma_3}{P_a}\right) \quad \text{Eq. 11}$$

547 In the aforementioned equation,  $\phi_p$  represents the utmost friction angle,  $\sigma_3$  denotes the minor  
 548 principal stress, and  $\phi_s$  signifies the internal friction angle at  $\sigma_3 = 100kPa$ . Pa corresponds to the  
 549 atmospheric pressure, while  $\Delta\phi$  represents the decrement in friction angle with respect to the  
 550 confining pressure for every tenfold increment in  $\sigma_3$ .

551 In the realm of geotechnical materials, the maximum dilation angle, denoted as  $\psi_p$ , is contingent

552 upon the applied confining pressure. In a general sense, the peak dilation angle,  $\psi_p$ , exhibits a  
553 diminishing trend as the confining pressure,  $\sigma_3$ , experiences an augmentation.

554

555 The supplementary data is available at:

556

## 557 **References**

- 558 1. Pinyol, N. and Alonso, E. "Design, construction, monitoring and modelling of Albagés Earth  
559 Dam: A case history", *Int. J. Civ. Eng.*, 17(3), pp. 501–513 (2019). DOI: 10.1007/s40999-018-  
560 0314-z
- 561 2. Aktarpour, A. and Salari, M. "The deformation mechanism of a high rockfill dam during the  
562 construction and first impounding", *Scientia Iranica*, 17(2), pp. 566-587 (2020). DOI:  
563 10.24200/sci.2018.20778
- 564 3. Feng, S., Wang, W., Hu, W., Deng, Y., Yang, J., Wu, S., Zhang, C. and Hoeg, K. "Design and  
565 performance of the Quxue asphalt-core rockfill dam", *Soils and Foundations*, 60(4), pp. 1036-  
566 1049 (2020). DOI: 10.1016/j.sandf.2020.06.008
- 567 4. Wang, L., Wu, C., Tang, L. et al. "Efficient reliability analysis of earth dam slope stability  
568 using extreme gradient boosting method", *Acta Geotech.*, 15(2), pp. 3135–3150 (2020). DOI:  
569 10.1007/s11440-020-00962-4
- 570 5. Wang, L., Wu, C., Gu, X. et al. "Probabilistic stability analysis of earth dam slope under  
571 transient seepage using multivariate adaptive regression splines", *Bull. Eng. Geol. Environ.*,  
572 79(3), pp. 2763–2775 (2020). DOI: 10.1007/s10064-020-01730-0
- 573 6. Liu, S., He, W., Sun, Y., Shen, C. and Wang, L. "Analysis of the behavior of a high earth-core  
574 rockfill dam considering particle breakage", *Computers and Geotechnics*, 157(2), p. 105320

- 575 (2023). DOI: 10.1016/j.compgeo.2023.105320
- 576 7. Alemie, N.A., Wosenie, M.D., Belew, A.Z., Kibret, E.A. and Ayele, W.T. "Performance  
577 evaluation of asphalt concrete core earth-rock fill dam relative to clay core earth-rock fill dam  
578 in the case of Megech Dam, Ethiopia", *Arabian Journal of Geosciences*, 14(24), p. 2712 (2021).  
579 DOI: 10.1007/s12517-021-09009-8
- 580 8. Zhang, W., Wu, J.H., Gu, X. et al. "Probabilistic stability analysis of embankment slopes  
581 considering the spatial variability of soil properties and seismic randomness", *J. Mt. Sci.*, 19(4),  
582 pp. 1464–1474 (2022). DOI: 10.1007/s11629-021-6981-2
- 583 9. Pan, J., Jiang, J., Cheng, Z., Xu, H. and Zuo, Y. "Large-scale true triaxial test on stress-strain  
584 and strength properties of rockfill", *International Journal of Geomechanics*, 20(1), p. 04019146  
585 (2020). DOI: 10.1061/(ASCE)GM.1943-5622.0001527
- 586 10. Han, H., Li, J., Shi, J. and Yang, C. "Influence of scale effect on strength and deformation  
587 characteristics of rockfill materials", *Materials*, 15(15), p. 5467 (2022). DOI:  
588 10.3390/ma15155467
- 589 11. Guo, Y., Chi, S., Mi, X. and Yan, S. "Experimental investigation of statistical characteristics  
590 of elastic mechanical parameters and strength indexes of rockfill particles", *Granular Matter*,  
591 25(2), p. 30 (2023). DOI: 10.1007/s10035-022-01302-x
- 592 12. Duncan, J. and Chang, C. "Nonlinear analysis of stress and strain in soils", *J. Soil Mech. Found.*  
593 *Div. ASCE*, 96(5), pp. 1629-1653 (1970). DOI: 10.1061/JSFEAQ.0001458
- 594 13. Shen, C., Liu, S. and Wang, L. "Elasto-plastic constitutive modelling of compacted rockfill  
595 materials: a physically based approach", *Géotechnique*, 71(4), pp. 1-13 (2021). DOI:  
596 10.1680/jgeot.21.00100
- 597 14. Guo, R. and Li, G. "Elasto-plastic constitutive model for geotechnical materials with strain-

- 598 softening behavior", *Comput. Geotech.*, 34(1), pp. 14–23 (2008). DOI:  
599 10.1016/j.cageo.2007.03.012
- 600 15. Escuder, I., Andreu, J. and Reche, M. "An analysis of stress-strain behaviour and wetting  
601 effects on quarried rock shells", *Can. Geotech. J.*, 42(1), pp. 51–60 (2005). DOI: 10.1139/t04-  
602 071
- 603 16. Vasistha, Y., Gupta, A.K. and Kanwar, V. "Medium triaxial testing of some rockfill materials",  
604 *J. Geotech. Eng.*, 18(4), pp. 923–964 (2013).
- 605 17. Kalantary, F., Sadoghi Yazdi, J. and Bazazzadeh, H. "Validation and application of  
606 evolutionary computational technique on disturbed state constitutive model", *Int. J. Civ. Eng.*,  
607 12(3), pp. 216-225 (2014). URL: <http://ijce.iust.ac.ir/article-1-845-en.html>
- 608 18. Naylor, D.J. "Collapse settlement–Some developments", In *Applications of Computational  
609 Mechanics in Geotechnical Engineering*, pp. 37-54 (2020). ISBN: 9781003078111
- 610 19. Alonso, E.E. and Oldecop, L.A. "Fundamentals of rockfill collapse", *Unsaturated Soils for  
611 Asia*, pp. 3-13 (2020). ISBN: 9781003078616
- 612 20. Ventini, R., Flora, A., Lirer, S., Mancuso, C. and Cammarota, A. "An experimental study of  
613 the behaviour of two rockfills accounting for the effects of degree of saturation", *EDP  
614 Sciences*, 195(3), p. 03033 (2020). DOI: 10.1051/e3sconf/202019503033
- 615 21. Wu, Y., Yin, Y., Zhang, B., Sun, X. and Yu, Y. "Unsaturated wetting deformation  
616 characteristics of a granite rockfill under rainfall conditions", *Canadian Geotechnical Journal*,  
617 59(10), pp. 1774-1792 (2022). DOI: 10.1139/cgj-2021-0047
- 618 22. Zhou, X., He, J., Chi, S. and Wang, J. "Study on collapse settlement and cracks of core wall  
619 rockfill dams under wetting deformation", *International Journal for Numerical and Analytical  
620 Methods in Geomechanics*, 47(1), pp. 106-128 (2023). DOI: 10.1002/nag.3462

- 621 23. Cheng, J., Ma, G., Zhang, G., Wang, Q. and Zhou, W. "Deterioration of mechanical properties  
622 of rockfill materials subjected to cyclic wetting–drying and wetting", *Rock Mechanics and*  
623 *Rock Engineering*, 56(4), pp. 2633-2647 (2023). DOI: 10.1007/s00603-022-03209-8
- 624 24. Hunter, G. "The pre- and post-failure deformation behaviour of soil slopes", (PhD Thesis),  
625 University of New South Wales, Australia (2003). DOI: 10.26190/unsworks/20980
- 626 25. Naylor, D., Maranha das Neves, E., Mattar, J. and Veiga Pinto, A. "Prediction of construction  
627 performance of Beliche Dam", *Géotechnique*, 36(3), pp. 359–376 (1986). DOI:  
628 10.1680/geot.1986.36.3.359
- 629 26. Oldecop, L. and Alonso, E. "Suction effects on rockfill compressibility", *Géotechnique*, 53(2),  
630 pp. 289-292 (2003). DOI: 10.1680/geot.2003.53.2.289
- 631 27. Mahin Roosta, R. and Alizadeh, A. "Simulation of collapse settlement in rockfill material due  
632 to saturation", *Int. J. Civ. Eng.*, 10(2), pp. 93-99 (2012). URL: [http://ijce.iust.ac.ir/article-1-](http://ijce.iust.ac.ir/article-1-521-en.html)  
633 [521-en.html](http://ijce.iust.ac.ir/article-1-521-en.html)
- 634 28. Mahinroosta, R., Aliadeh, A. and Gatmiri, B. "Simulation of collapse settlement of first filling  
635 in a high rockfill dam", *Engineering Geology*, 187(2), pp. 32-44 (2015). DOI:  
636 10.1016/j.enggeo.2014.12.013
- 637 29. Charles, J. "Geotechnical properties of coarse-grained soils", *Proc. of the 12th Int. Conf. on*  
638 *Soil Mechanics and Foundation Engineering*, General Report, Discussion Session 8, pp. 2495–  
639 2519 (1989).
- 640 30. Oldecop, L. and Alonso, E.E. "Fundamentals of rockfill time-dependent behaviour", *Proc. 3rd*  
641 *Int. Conf. on Unsaturated Soils*, Recife, 2(1), pp. 793–798 (2002).
- 642 31. Osses, R., Majdanishabestari, K., Ovalle, C. and Pineda, J. "Testing and modelling total suction  
643 effects on compressibility and creep of crushable granular material", *Soils and Foundations*,

- 644 61(6), pp. 1581-1596 (2021). DOI: 10.1016/j.sandf.2021.09.006
- 645 32. Xu, M., Jin, D. and Zhou, W. "An experimental study on the time-dependent behavior of  
646 crushable granular materials using 3D-printed particles", *Acta Geotechnica*, 17(1), pp. 93-104  
647 (2022). DOI: 10.1007/s11440-021-01232-7
- 648 33. Zhou, X., Shen, F. and Berto, F. "Experimental study on triaxial creep behavior of red  
649 sandstone under different pore pressures based on ultrasonic measurement", *Fatigue &  
650 Fracture of Engineering Materials & Structures*, 45(8), pp. 2388-2402 (2022a). DOI:  
651 10.1111/ffe.13753
- 652 34. Zhou, X., Pan, X. and Berto, F. "A state-of-the-art review on creep damage mechanics of  
653 rocks", *Fatigue & Fracture of Engineering Materials & Structures*, 45(3), pp. 627-652 (2022b).  
654 DOI: 10.1111/ffe.13625
- 655 35. Bauer, E. "Constitutive modelling of wetting deformation of rockfill materials", *Int. J. Civ.  
656 Eng.*, 17(1), pp. 481-486 (2019). DOI: 10.1007/s40999-018-0327-7
- 657 36. Nobari, E. and Duncan, J. "Effect of reservoir filling on stresses and movements in earth and  
658 rockfill dams", Report TE-72, University of California, Department of Civil Engineering  
659 (1972).
- 660 37. Vermeer, P. and De Borst, R. "Non-associated plasticity for soils, concrete and rock", *Heron*,  
661 29(3), pp. 12-27 (1984). URL: [https://resolver.tudelft.nl/uuid:4ee188ab-8ce0-4df3-adf5-  
662 9010ebfaabf0](https://resolver.tudelft.nl/uuid:4ee188ab-8ce0-4df3-adf5-9010ebfaabf0)
- 663 38. Rowe, P. "Stress-dilatancy, earth pressure and slopes", *J. Soil Mech. Found. Div. ASCE*, 89(5),  
664 pp. 37-61 (1963). DOI: 10.1061/JSFEAQ.0000520
- 665 39. Itasca Consulting Group. "FLAC3D, User's manuals", Itasca Consulting Group, Minnesota  
666 (2012).

667 40. Hasanzadehshooiili, H.M., Lakirouhani, A. and Oshtaghi, V. "Using artificial neural network  
668 (ANN) in prediction of collapse settlements of sandy gravels", Arab. J. Geosci., 7(6), pp. 2303–  
669 2314 (2014). DOI: 10.1007/s12517-013-0858-9

670

### 671 **Figure Captions**

672 Fig. 1. The variation of settlement of surface survey points on the dam body in the maximum cross-  
673 section from the end of the first impounding, during the long-term period

674 Fig. 2. The variation of horizontal displacements (perpendicular to the dam axis) of surface survey  
675 points on the dam body in the maximum cross-section from the end of the first impounding during  
676 the long-term period (a positive value means displacement toward upstream)

677 Fig. 3. Division of embankment for analysis of surface deformations during the post-construction  
678 period

679 Fig. 4. Settlements measured at the survey points installed in the lower gallery of the foundation

680 Fig. 5. Vertical profile of relative horizontal displacements in downstream inclinometers

681 Fig. 6. 3D numerical model and grid generation of the dam and foundation

682 Fig. 7. Pore water pressure (September 2016)

683 Fig. 8. Effective vertical stress (September 2016)

684 Fig. 9. Tensile stress (September 2016)

685 Fig. 10. relative settlement to the end of the first impounding (September 2016)

686 Fig. 11. Relative horizontal displacement to the end of first impounding (September 2016)

687 Fig. 12. Relative vertical displacement to the end of first impounding (September 2016)

688 Fig. 13. Relative horizontal displacement to the end of first impounding (September 2016)

689 Fig. 14. Relative surface settlement to the end of first impounding (September 2016)

690 Fig. 15. Relative surface horizontal displacement to the end of first impounding (September 2016)

691 Fig. 16. Relative horizontal displacement parallel to the end of first impounding to axis dam  
692 (September 2016)

693 Fig. 17. Relative deformed mesh to the end of first impounding with scale 10:1 (September 2016)

694 Fig. 18. Relative deformed mesh to the end of first impounding with scale 10:1 (September 2016)

695 Fig. 19. Schematic sketch of long-term deformation mechanism of the dam

### 696 **Table Captions**

697 Table 1. Absolute pore water pressure ratio,  $r_u$ , and the ratio of total vertical stress to total  
698 horizontal stress,  $r_k$ , at the core in the instrumented main chainage

699 Table 2. different regions parameters of the embankment

700 Table 3. The rock mass parameters

701 Table 4. The parameters of the creep model for dam shell

702 Table 5. Data of different stages of impounding

703

704

705

706

707

### 708 **Figure List**



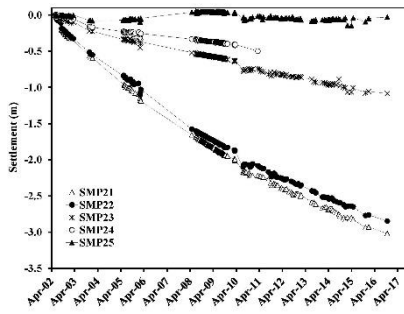


Fig. 1. The variation of settlement of surface survey points on the dam body in the maximum cross-section from the end of the first impounding, during the long-term period

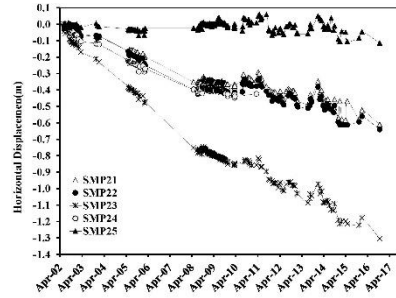


Fig. 2. The variation of horizontal displacements (perpendicular to the dam axis) of surface survey points on the dam body in the maximum cross-section from the end of the first impounding during the long-term period (a positive value means displacement toward upstream)

709

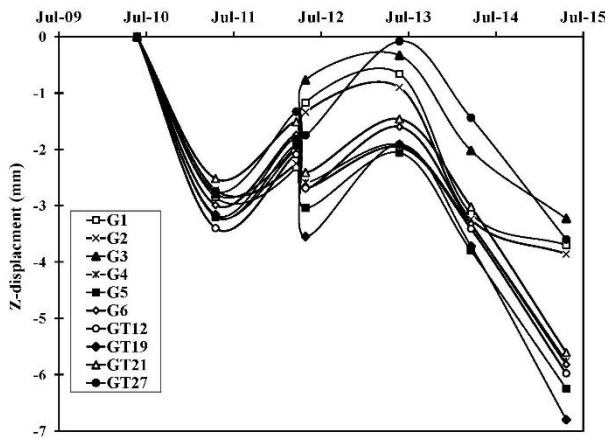


Fig. 4. Settlements measured at the survey points installed in the lower gallery of the foundation

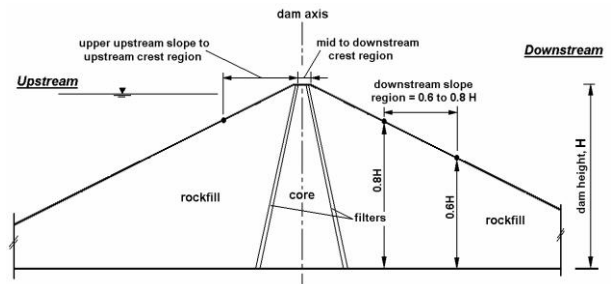


Fig. 3. Division of embankment for analysis of surface deformations during the post-construction period

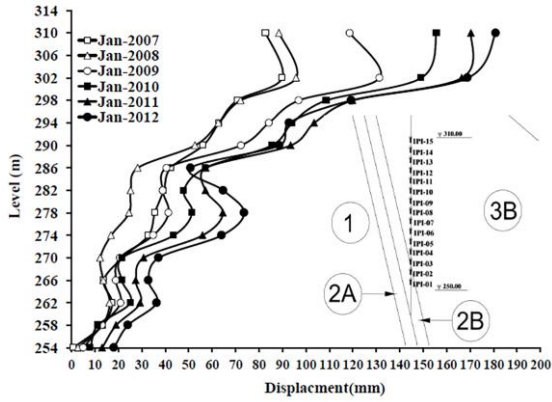


Fig. 5. Vertical profile of relative horizontal displacements in downstream inclinometers

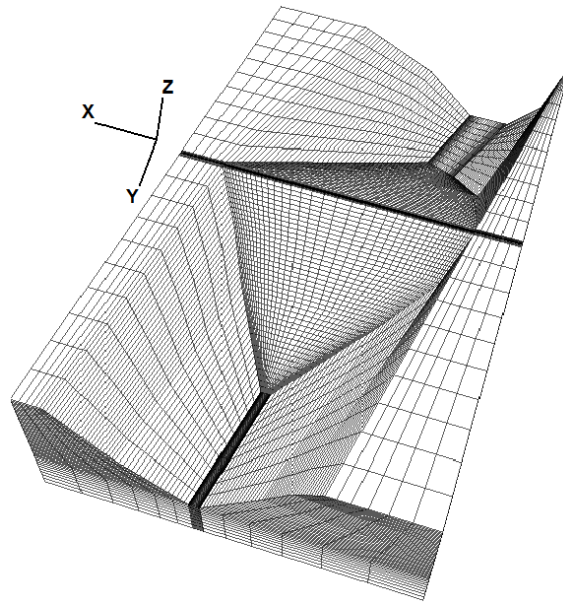


Fig. 6. 3D numerical model and grid generation of the dam and foundation

710

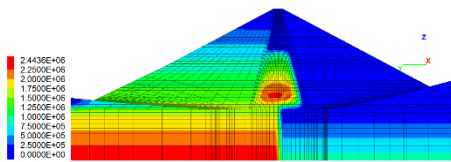


Fig. 7. Pore water pressure (September 2016)

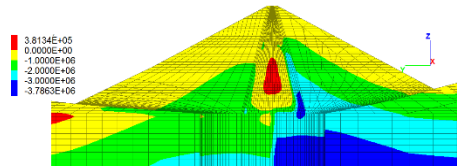


Fig. 8. Effective vertical stress (September 2016)

711

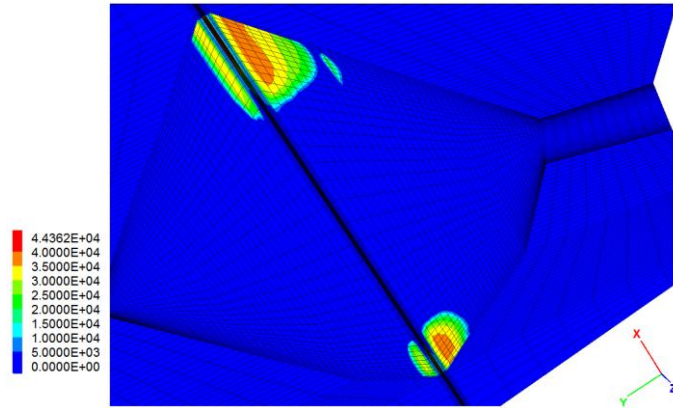


Fig. 9. Tensile stress (September 2016)

712

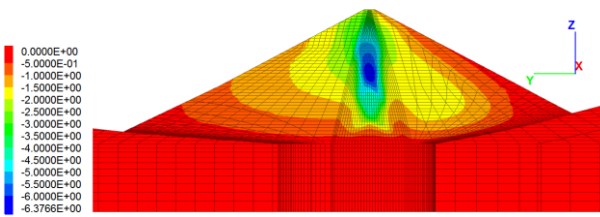


Fig. 10. relative settlement to the end of the first impounding (September 2016)

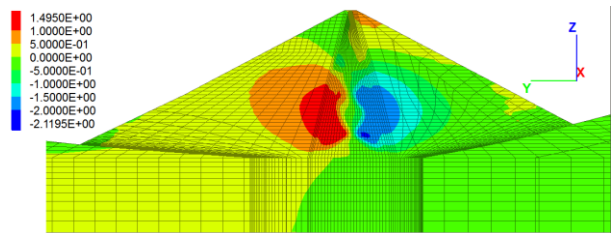


Fig. 11. Relative horizontal displacement to the end of first impounding (Septamter2016)

713

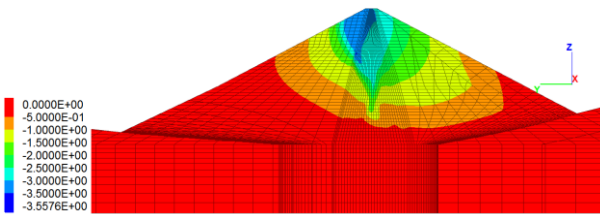


Fig. 12. Relative vertical displacement to the end of first impounding (September 2016)

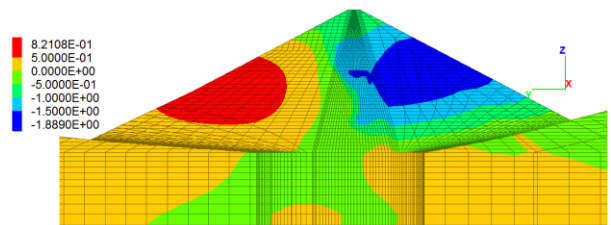


Fig. 13. Relative horizontal displacement to the end of first impounding (September 2016)

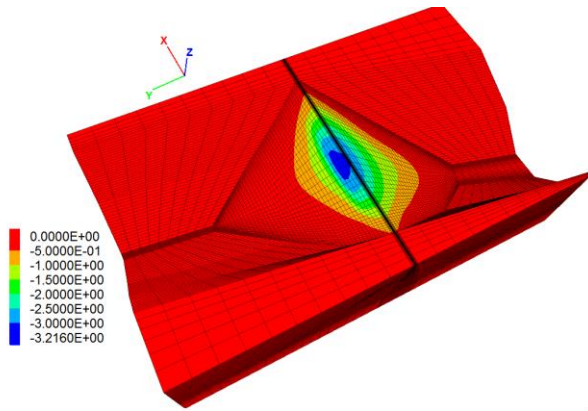


Fig. 14. Relative surface settlement to the end of first impounding (September 2016)

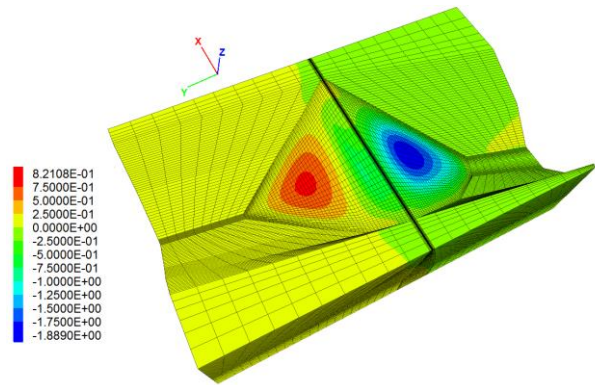


Fig. 15. Relative surface horizontal displacement to the end of first impounding (September 2016)

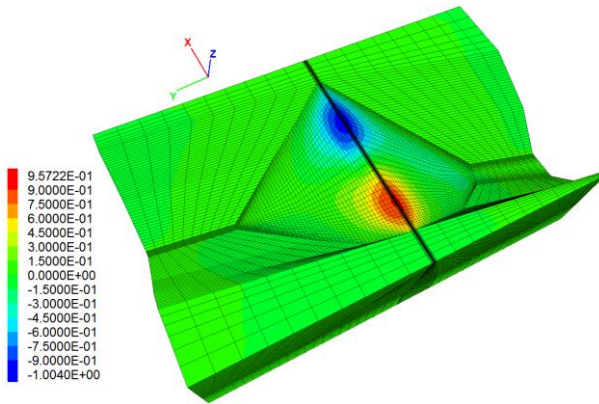


Fig. 16. Relative horizontal displacement parallel to the end of first impounding to axis dam (September 2016)

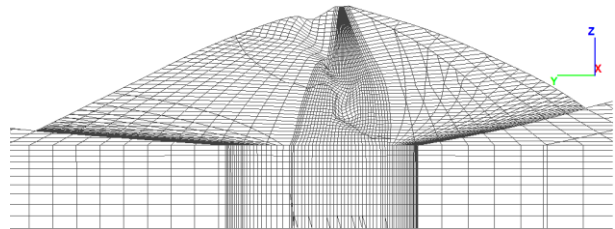


Fig. 17. Relative deformed mesh to the end of first impounding with scale 10:1 (September 2016)

714

715

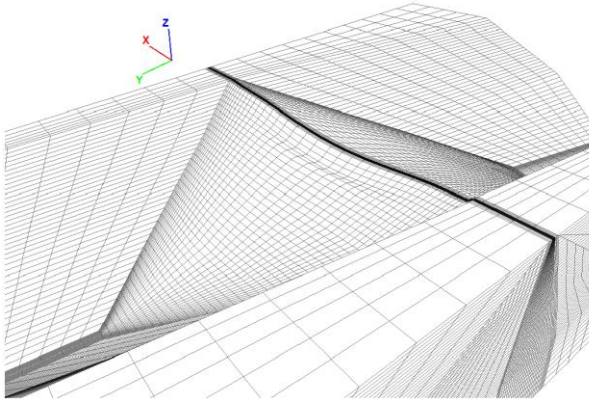


Fig. 18. Relative deformed mesh to the end of first impounding with scale 10:1 (September 2016)

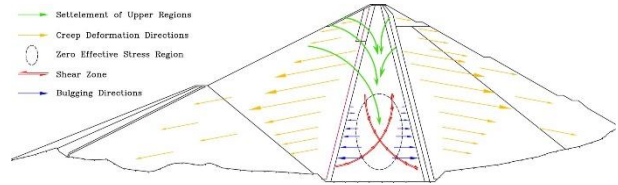


Fig. 19. Schematic sketch of long-term deformation mechanism of the dam

716 **Table List**

Table 1. Absolute pore water pressure ratio,  $r_u$ , and the ratio of total vertical stress to total horizontal stress,  $r_k$ , at the core in the instrumented main chainage

Loc.		2003	2004	2005	2006	2007	2008	2009	2010	2011	2012	2013	2014	2016
C1	$r_k$	1	1	0.99	0.98	0.97	0.96	0.95	-	-	-	-	-	-
	$r_u$	0.98	0.97	0.97	-	-	-	-	-	-	-	-	-	-
C2	$r_k$	0.74	0.74	0.73	0.69	0.69	-	-	-	-	-	-	-	-
	$r_u$	0.9	0.92	0.93	0.92	0.92	0.92	0.92	-	-	-	0.9	0.89	0.88
C3	$r_k$	1.03	1.02	-	-	-	-	-	-	-	-	-	-	-
	$r_u$	1.03	1.02	1.01	-	-	-	-	-	-	-	-	-	-
C4	$r_k$	1	1.01	1.03	1.05	1.08	1.05	1.07	-	-	-	-	-	-
	$r_u$	1.04	1.04	1.06	1.04	1.06	1.05	1.04	-	-	-	-	-	-
C5	$r_k$	-	-	-	-	-	-	-	-	-	-	-	-	-
	$r_u$	0.58	0.82	0.81	0.8	0.78	0.77	0.76	-	-	-	-	-	-
C6	$r_k$	1	1	0.99	0.98	0.97	0.96	0.95	-	-	-	-	-	-
	$r_u$	0.98	0.97	0.97	-	-	-	-	-	-	-	-	-	-

Table 2. The mechanical and flow parameters of the different regions of the embankment

Zone	3A,3C (Saturated)	3A,3C(dry)	3B	2A	2B,2C	Core
$\rho_d(\frac{gr}{cm^3})$	2	2	2	1.9	2.1	1.89
$n$	0.74	-0.12	0.05	1	0	0.8
$K$	556	3672	422	138	1663	120
$V$	0.1	0.1	0.2	0.15	0.1	0.15
$C(\frac{kN}{m^2})$	25	65	40	10	20	30
$\varepsilon_f(\%)$	6	6	7	8.5	8.5	10
$I_d$	$0.77 \cdot (\frac{\sigma_3}{P_a}) + 0.25$	5	2.5	3.5	1	1
$R_d$	1	1	1	1	1	1
$\phi_p$	$55 - 11.1 \cdot \log(\frac{\sigma_3}{P_a})$	$51.3 - 7 \cdot \log(\frac{\sigma_3}{P_a})$	$42.23 - 0.64 \cdot \log(\frac{\sigma_3}{P_a})$	$45 - 6.64 \cdot \log(\frac{\sigma_3}{P_a})$	$46.36 - 4.82 \cdot \log(\frac{\sigma_3}{P_a})$	30
$\psi_p$	$\begin{cases} 5.5 & \frac{\sigma_3}{P_a} \leq 3 \\ 0.0 & \frac{\sigma_3}{P_a} > 3 \end{cases}$	$\begin{cases} 1.5 & \frac{\sigma_3}{P_a} \leq 6 \\ 0.0 & \frac{\sigma_3}{P_a} > 6 \end{cases}$	0	0	$1.15 - 0.83 \cdot \log(\frac{\sigma_3}{P_a})$	0
$\phi_0$	$41.9 - 30 \cdot \log(\frac{\sigma_3}{P_a})$	$33.6 - 16.6 \cdot \log(\frac{\sigma_3}{P_a})$	$34.2 - 19.93 \cdot \log(\frac{\sigma_3}{P_a})$	$39.7 - 2.7 \cdot \log(\frac{\sigma_3}{P_a})$	$30 - 2.6 \cdot \log(\frac{\sigma_3}{P_a})$	0
$K_{int} (cm/s)$	$1 \times 10^{-1}$	$1 \times 10^{-1}$	$1 \times 10^{-4}$	$2 \times 10^{-2}$	$1 \times 10^{-2}$	Eq.(1)

718

Table 3. The rock mass parameters

Model	$\rho_d(\frac{gr}{cm^3})$	E(GPa)	$\nu$	$K_{int} (cm/s)$
Linear elastic	2.4	2	0.25	$5 \times 10^{-8}$

719

720

Table 4. The parameters of the creep model for dam shell

Parameter	3A,3C,dry	3A, saturated	3B
Bulk(K)	With the help of parameters (K, n, v) in Table 2		
$G^M$			
$C \left( \frac{kN}{m^2} \right)$	65	25	40
$\Psi$	$\begin{cases} 1.5 & \frac{\sigma_3}{P_a} \leq 6 \\ 0.0 & \frac{\sigma_3}{P_a} > 6 \end{cases}$	$\begin{cases} 5.5 & \frac{\sigma_3}{P_a} \leq 3 \\ 0.0 & \frac{\sigma_3}{P_a} > 3 \end{cases}$	0
$\phi$	$51.3 - 7. \log\left(\frac{\sigma_3}{P_a}\right)$	$55 - 11.1 \log\left(\frac{\sigma_3}{P_a}\right)$	$42.23 - 0.64. \log\left(\frac{\sigma_3}{P_a}\right)$
Tension( $\frac{kN}{m^2}$ )	0	0	0
$G^K$	Approximately, 10% of $G^M$		
$\eta^K$ (GPa.s)	$1 \times 10^8$	$1.1 \times 10^8$	$1.42 \times 10^8$
$\eta^M$ (GPa.s)	$2.5 \times 10^6$	$2.9 \times 10^6$	$3.3 \times 10^6$

721

Table 5. Data of different stages of impounding

Stage of impounding	1	2	3	4	5	6
Range of reservoir water level (m)	255- 288	288- 312	312- 328	328- 335	335- 357	357- 371
Duration (day)	1	9	49	12	446	34
$C_c$	0.1	0.1	0.8	0.8	0.8	0.8

722

723

724

725 **First Author (Morteza Salari):**

726 Morteza Salari has graduated in MSc of Geotechnical Engineering from Ferdowsi university of Mashhad  
 727 in 2009. He is now an Expert in Maharab Consulting Engineering Company in Mashhad. Also, he has some

728 experiences on the field of embankment dam engineering for the 11 years. Also, he is a PhD student in  
729 Ferdowsi university of Mashhad.

730 **Second Author (Ali Akhtarpour):**

731 Dr Ali Akhtarpour was graduated from polytechnic university of Tehran in BSc of civil engineering, MSc  
732 (Under supervision of Dr Abbas Soroush) and PhD (Under supervision of Dr Ali Khodaii) of geotechnical  
733 engineering in 2000, 2003 and 2011 respectively. Now he is a staff member (Associate Prof.) of engineering  
734 faculty in the Ferdowsi University of Mashhad. Also he has some experiences on the embankment dam  
735 design, monitoring and numerical modelling for more than 20 years. You can find more about publications  
736 and interesting subject area in his personal homepage as below:

737 <http://akhtarpour.profcms.um.ac.ir/>

738 **Third Author (Sajjad Khosravi):**

739 Sajjad Khosravi is a geotechnical engineer with a Master's degree in Geotechnical Engineering from Iran  
740 University of Science and Technology. With over four years of research experience, he has recently  
741 concluded his role as a Research Assistant at Ferdowsi University of Mashhad. His areas of expertise  
742 include machine learning methods and numerical modeling in geotechnical engineering. He has also  
743 contributed to the design of two tunnel shield lines in Mashhad and authored multiple papers on machine  
744 learning and numerical modeling in geotechnical engineering.

745